Dalton Transactions

ROYAL SOCIETY OF CHEMISTRY

PAPER

View Article Online
View Journal | View Issue

Cite this: *Dalton Trans.*, 2025, **54**, 17102

Interplay of dual-site metal disorder on the thermodynamic stability and electronic structures of Cu(I)-containing molybdovanadate and tungstovanadate compounds

Machima Mongkhonratanachai, Subhendu Jana and Paul A. Maggard *

Compounds combining Cu(I) and early transition-metal cations have attracted much attention as small-bandgap semiconductors. However, synthetic progress and new discoveries in these systems have been inhibited by their limited stability. Two new Cu(I)-molybdovanadates and one new Cu(I)-tungstovanadate have been synthesized in the Cu(I)–V(V)–M(VI)–O (M = Mo, W) systems, $CuVMoO_6$ (**1**), $Cu_{1.51(1)}V_{3.57(1)}Mo_{0.43(1)}O_{11}$ (**2**) and $Cu_{1.59(1)}V_{3.52(1)}W_{0.48(1)}O_{11}$ (**3**). Their structures were characterized by single crystal X-ray diffraction to contain layers of distorted VO_6/MO_6 octahedra with their mixed occupancy driven by the similar atomic radii of the early transition-metal cations. Interlayer sites are occupied by uncommon octahedrally-coordinated Cu, and in **2** and **3** by ~25–30% occupancy of distorted tetrahedral sites. Electronic structure calculations show that while **1** is stable *versus* binary oxides, the $CuVWO_6$ analogue is not stable and could not be synthesized. The isostructural compounds, **2** and **3**, also exhibited greater stability when the CuO_4 occupied sites are directly bridged to the VO_6 octahedra rather than the MoO_6/WO_6 octahedra. A small optical bandgap of ~0.8 eV was measured for **1**, with **2** and **3** being undetectable and calculated to be semi-metals. Thus, these results provide deeper insights into the energetic driving forces underlying the successful synthesis of Cu(I)-containing oxides.

Received 20th September 2025,
Accepted 27th October 2025

DOI: 10.1039/d5dt02255j

rsc.li/dalton

1. Introduction

Research investigations into new small-bandgap semiconductors have been expanding with the aim to increase their stability and efficiency in the capture and conversion of solar energy.[1,2] In particular, Cu(I)-containing oxides have shown significant promise in their photoelectrochemical properties as p-type electrodes, such as being useful for driving the reduction of water to molecular hydrogen or the reduction of carbon dioxide to ethanol.[3–6] The optical bandgaps of Cu(I) oxides frequently occur within the visible-light energy range of ~1.5 to 3.0 eV as a result of the formation of a higher-energy valence band derived from the filled $3d^{10}$ orbitals.[7] This leads to a reduced energetic distance to the conduction-band states stemming from the unfilled orbitals of an early transition-metal or main group cation such as V(V), W(VI) or Sn(IV), for example, as reported in Cu_3VO_4, Cu_2WO_4 and Cu_2SnO_3 and many others.[6–12] However, relatively few new examples have been reported, which have likely been limited by the fact that the majority of Cu(I)-containing oxides are thermodynamically unstable with respect to their constituent binary oxides.[7]

Synthetic techniques which utilize low temperatures and flux-mediated reaction conditions have previously proven effective in the preparation of many Cu(I)-containing multinary oxides. This has included the relatively few known Cu(I)-containing niobates, vanadates and tantalates in each of their respective chemical systems.[6,8,11] The photocatalytic activities of members of this family as p-type electrodes have been shown to stem from the extrusion of the Cu(I) cations upon heating, concurrent with oxidation and formation as CuO nano-islands at the crystallite surfaces. While the predominant range of their visible-light bandgap spans ~2.0 to 2.6 eV, even smaller bandgaps around 1.5 eV are needed for use in solar cells that can absorb a broader cross-section of solar energy. The only known examples exhibiting small bandgaps of ~1.2 eV to 1.4 eV have been reported for Cu_3VO_4,[8] $CuNb_3O_8$,[13] and $Cu_2Nb_8O_{21}$.[14] These all represent examples of thermodynamically unstable semiconductors, with their slow decomposition resulting from complete phase segregation, such as given by the following: $2Cu_3VO_4 \rightarrow 3Cu_2O + V_2O_5$. Furthermore, the chemical compositions and structural features, including the coordination environment of the Cu(I) cation and the extended connectivity, leading to their small

Department of Chemistry and Biochemistry, Baylor University, Waco, Texas, 76798, USA. E-mail: Paul_Maggard@baylor.edu

bandgaps have not been well understood. Thus, the lack of Cu(I)-containing multinary oxides possessing thermodynamic stability and small bandgaps represents a major current limitation.

Reported herein is the discovery of three new Cu(I)-containing compounds during synthetic explorations of the quaternary Cu–V–Mo–O and Cu–V–W–O chemical systems, $CuVMoO_6$ (**1**), $Cu_{1.51(1)}V_{3.57(1)}Mo_{0.43(1)}O_{11}$ (**2**) and $Cu_{1.59(1)}V_{3.52(1)}W_{0.48(1)}O_{11}$ (**3**). These represent the first known compounds within their respective systems. The structures have been characterized by single crystal X-ray diffraction techniques to consist of layered structural features with mixed-site V/Mo and V/W occupancies, and in the structures of **2** and **3**, the occurrence of complex, Cu-site disorder. These exhibit some of the smallest optical bandgaps reported for Cu(I)-containing multinary oxides, occurring at 0.8 eV for **1** and less than 0.5 eV for **2** and **3**. Electronic structure calculations show that all three represent some of the first known examples of Cu(I)-quaternary oxides that are thermodynamically stable with respect to the binary oxides. Thus, these results demonstrate a promising new pathway in the mixed-metal Cu(I)-containing systems for the attainment of small bandgaps and thermodynamically-stable structures.

2. Experimental

2.1. Synthetic methods

2.1.1. Starting materials. The products were synthesized by conventional solid-state methods starting from the following reagents. Cu metal powder (Thermo Scientific, 99.9% purity), CuO (Thermo Scientific, 99.995% purity), Cu_2O (STREM Chemical Inc., 99.9% purity), V_2O_5 (BeanTown chemical Inc., 99.9% purity), MoO_3 (BeanTown Chemical, 99.9995% purity), and WO_3 (Thermo scientific, 99.998% purity). All materials were handled in ambient atmosphere.

2.1.2. Synthetic procedures. Black colored single crystals of $CuVMoO_6$ (**1**) were prepared by high-temperature reaction of stoichiometric amounts of Cu, CuO, V_2O_5, and MoO_3 that were loaded in 1 : 1 : 1 : 2 molar ratio. The powders were ground in a mortar and pestle and transferred to a fused-silica tube that was flame sealed under vacuum. This tube was transferred to a high temperature box furnace and heated to 850 °C at 200 °C per hour and held at this temperature for 48 h, followed by slow cooling at a rate of 6 °C per hour to 550 °C. Subsequently, the reaction was cooled radiatively to room temperature. The black colored single crystals of $Cu_{1.51(1)}V_{3.57(1)}Mo_{0.43(1)}O_{11}$ (**2**) and $Cu_{1.59(1)}V_{3.52(1)}W_{0.48(1)}O_{11}$ (**3**) were prepared starting from Cu_2O, V_2O_5, and MoO_3 in a molar ratio of 1 : 1.7 : 1.2 and Cu_2O, V_2O_5, and WO_3 in a molar ratio of 1 : 2.1 : 0.5, respectively. The powders were ground and heated according to the same temperature profile described for **1**. The crystal morphologies of **1** and **3** exhibited black shiny needle shapes with a high purity for **1** but only about 50% purity for **3**. The crystal morphology of **2** was found to be platelet shaped in about 50% purity. Repeated steps of regrinding and reheating did not improve the purity level of the product.

2.2. Characterization techniques

2.2.1. Single crystal X-ray diffraction (SCXRD) characterization. Selected crystals of **1**, **2**, and **3** were selected for SCXRD using monochromatized Mo-Kα radiation of a Rigaku XtaLAB Synergy diffractometer at room temperature. The datasets were collected using a HyPix Arc 100 detector. The crystals were individually fixed onto transparent loops under viscous Paratone N oil and the loops were each mounted on a goniometer head. The diffraction intensity data were recorded using CrysalisPro.[15] The SHELXT software suite was used to solve and refine the single crystal X-ray data sets by direct methods.[16] Compound **1** showed six crystallographically-independent atomic sites. Each peak was assigned to respective elements based on coordination environments and intensity. The least squares method in SHELXL provided occupancies, scale factors, atomic positions, extinction corrections, weight corrections, and anisotropic displacement parameters. The final solution established the full occupancies of Cu1, O1, O2, O3 along with one mixed Mo1/V1 site that yielded refined occupancies of ~48% and ~52% for Mo1 and V1, respectively. Thus, these values were within standard deviation and fixed to 50% for charge balancing. For the structure of **2**, the final refinement converged to the composition $Cu_{1.51(1)}V_{3.57(1)}Mo_{0.43(1)}O_{11}$ which contained eight fully occupied sites (V2, Cu2, O5, O2, O1, O6, and O3) along with three partially occupied sites. V1 and Mo1 at the same atomic position gave refined occupancies of 78.3% and 21.7%, respectively, and a partial Cu1 occupancy of 25.3%. The structure of **3** was refined to have the $Cu_{1.59(1)}V_{3.52(1)}W_{0.48(1)}O_{11}$ chemical composition with eight fully occupied sites, as described for **2**, but V1 and W1 at the atomic same position were refined to occupancies of 76.2% and 23.8%, respectively. The Cu1 site was refined to 29.3% occupancy. PLATON was used to check the symmetry of the final structure.[17] Atomic positions in the structures were standardized using the STRUCTURE TIDY program.[18] Selected refinement details of each compound are listed in Tables 1, S1, S4 and S7, including the Wyckoff positions, site symmetries, and occupancies. Further details are given in the SI.

2.2.2. Powder X-ray diffraction (PXRD) characterization. The bulk powder of **1** was ground by a mortar and pestle and its PXRD data was taken on a Bruker D2 Phaser instrument operating with a sealed tube Cu-Kα radiation source at a voltage of 45 kV and a current of 40 mA. Data collection proceeded with a 0.013° of step size at an angular 2θ range of 5° to 75° on a stage mounted in a Bragg-Bentano sample geometry at room temperature in an ambient atmosphere. Black crystals for PXRD data collection of **2** and **3** were mechanically separated for measurements on a Rigaku XtaLAB Synergy diffractometer operated using Cu-Kα source (λ = 1.54056 Å) and a HyPix Arc 100 detector. Data were collected in an angular 2θ range of 3.57° to 123.78° with an exposure time of 300 s per frame, a detector distance 60 mm, and 360° θ-scans.

2.2.3. Spectroscopic characterization methods. Crystals from the SCXRD data sets were subsequently transferred to adhesive carbon tape on top of an aluminum sample holder.

Table 1 Selected crystallographic refinement details for the crystal structures of $CuVMoO_6$ (**1**) $Cu_{1.51(1)}V_{3.57(1)}Mo_{0.43(1)}O_{11}$ (**2**), and $Cu_{1.59(1)}V_{3.52(1)}W_{0.48(1)}O_{11}$ (**3**)[a]

Refinement parameters	1	2	3
Space group		$C2/m$	
a (Å)	9.4454(9)	15.3222(9)	15.2890(8)
b (Å)	3.6768(2)	3.6326(2)	3.6380(2)
c (Å)	6.4863(5)	7.3249(4)	7.3307(3)
β (°)	111.483(8)	104.843(5)	104.709(5)
V (Å^3)	209.61(3)	394.10(4)	394.38(4)
Z	2	2	2
ρ (gm m^{-3})	4.855	4.171	4.578
μ (mm^{-1})	10.09	8.78	15.17
R (F)[b]	0.027	0.042	0.043
R_w (F_o^2)[c]	0.056	0.114	0.107
S	1.05	1.12	1.12
No. of reflections	899	1998	1843
No. of independent reflections	367	637	691
δF (e Å^{-3})	0.84, −0.86	1.38, −1.82	2.00, −2.10

[a] λ = 0.71073 Å, T = 300(2) K. [b] $R(F) = \sum||F_o| - |F_c||/\sum|F_o|$ for $F_o^2 > 2\sigma(F_o^2)$. [c] $R_w(F_o^2) = \{\sum[w(F_o^2 - F_c^2)^2]/\sum wF_o^4\}^{1/2}$. For $F_o^2 + < 0$, $w = 1/[\sigma^2(F_o^2) + (0.022P)^2]$, $w = 1/[\sigma^2(F_o^2) + (0.0547P)^2 + 7.0779P]$, and $w = 1/[\sigma^2(F_o^2) + (0.0398P)^2 + 9.9575P]$ for the crystal structures of **1**, **2** and **3**, respectively, where $P = (F_o^2 + 2F_c^2)/3$.

The samples were imaged using Scanning Electron Microscopy on a JEOL SEM 6010LA instrument and using energy dispersive X-ray (EDX) spectroscopy for elemental analysis. EDX analysis was conducted at 30 keV. The L line of W and Mo and the K lines of Cu and V were used to calculate their molar percentages. Molar percentages were averaged from 3 maps and 16 spots in **1**, 3 maps and 21 spots for **2**, and 1 map and 8 spots in **3**. Solid-state UV-Vis diffuse reflectance spectroscopy (DRS) were collected using the powder of **1** to probe its optical absorption in the wavelength range of ~2000 nm (0.62 eV) to 250 nm (4.96 eV) by a JASCO V-770 UV-Vis-NIR spectrophotometer. The reflectance data were transformed to absorption data using the Kubelka–Munk equation ($\alpha/S = (1 - R^2)/2R$), where R, S, and α are reflectance and scattering coefficients, and absorption coefficients, respectively.[19] Tauc plots were used to evaluate the direct or indirect absorption edges with the following eqn (1):[20]

$$(\alpha h\nu)^n = A(h\nu - E_g) \quad (1)$$

where E_g, A, h, and ν represent the band gap, proportionality constant, Planck's constant and frequency of light, respectively. The plots of the direct or indirect band transition are indicated when n = 2 and $\frac{1}{2}$, respectively.

2.3. Electronic structure calculations

Electronic structure calculations of **1**, **2** and **3** were carried out as implemented in the Vienna *Ab Initio* Simulation Package (VASP; ver. 6.4.2) software using the project augmented wave method (PAW).[21,22] The electron exchange and correlation were treated according to the Perdew–Burke–Ernzerhof (PBE) functional based on the generalized gradient approximation. Selected PAW pseudopotentials for inclusion of specific valence sublevels were those for O (2s, 2p), Cu (4s, 3d, 4p) Mo (4s, 4p, 4d, 5s) and W (5s, 5p, 5d, 6s). Structural disorder of the V/Mo and V/W sites was modeled by doubling the *b*-axis of each structure, followed by a random occupation of their atomic sites to give a 1 : 1 (V-to-Mo) molar ratio for **1** and a 1 : 7 (V to Mo/W) molar ratio for **2** and **3**. Partial occupancies (~25%) of the Cu1 atomic site in **2** and **3** were treated with the Cu atom occupying one out of four possible sites in each. This Cu atom could be oxygen-bridged to either the Mo/W cation or the V cation within each structure, thus defining the respective α and β polymorphs of each structure. The final compositions of the superstructures were consistent with the structural refinements. Initially, full geometry relaxations, symmetry-constrained in their respective space groups, were executed with a cutoff energy of 520 eV at an electronic energy convergence set to 10^{-8} eV, until the norm on all atoms fell below 0.01 eV Å^{-1}. Next, density-of-states calculations were performed using 4 × 10 × 4 *k*-point meshes (total: 84 *k*-points) for **1** and the hypothetical $CuVWO_6$, and with 5 × 11 × 11 *k*-point meshes (total: 168 *k*-points) for **2** and **3**. Subsequently, spin-polarized band structures were calculated using 10 *k*-point intersections along each high-symmetry Brillouin zone direction, *i.e.*, Γ–X|Y–Γ–Z|R_2–Γ–T_2|U_2–Γ–V_2 for **1** and Γ–Z–D–B–Γ–A–E–Z–C_2–Y_2–Γ for **2** and **3**, as determined by Seek-path.[23] The Crystal Orbital Hamilton Populations (COHP) of the pairwise Cu–O, Mo–O, W–O interactions were analyzed with the use of the LOBSTER (Local-Orbital Suite Towards Electronic-Structure Reconstruction) software package version 5.1.1.[24–26]

3. Results and discussion

3.1. Synthesis and crystal structures

Black, lustrous crystals of the new quaternary Cu(I)-containing compounds, $CuVMoO_6$ (**1**), $Cu_{1.51(1)}V_{3.57(1)}Mo_{0.43(1)}O_{11}$ (**2**) and $Cu_{1.59(1)}V_{3.52(1)}W_{0.48(1)}O_{11}$ (**3**), were synthesized at 850 °C for 48 hours in evacuated, sealed, fused-silica tubes. All crystals were stable in the air over a period of several weeks. Energy dispersive spectroscopy on crystals of the respective compounds yielded molar percentages (excluding oxygen, which overlapped with vanadium) consistent with their refined compositions, Fig. S4 to S6 in the SI. Results of the single-crystal structure refinements showed that each crystallized in the monoclinic centrosymmetric space group $C2/m$ with the unit cell dimensions listed in Table 1. All three compounds are the first to be discovered and reported in the synthetic exploration of the Cu–V–Mo–O and Cu–V–W–O chemical systems, with the latter two (**2** and **3**) representing a new crystal-structure type.

The structure of **1**, illustrated in Fig. 1, can be viewed as a derivative of the parent $LiVMoO_6$ compound, with the replacement of Li by Cu. Briefly, the structure contains layers of $[VMoO_6]^{n-}$ that are comprised of a single symmetry-unique V/Mo site that is coordinated in a highly-distorted octahedron with (V/Mo)–O distances of 1.675(3) Å, 1.725(3) Å, 1.9252(9) Å (×2), 2.123(3) Å and 2.434(3) Å. Each $(V/Mo)O_6$ octahedron is edge-shared to neighboring octahedra to form a zigzag chain, as

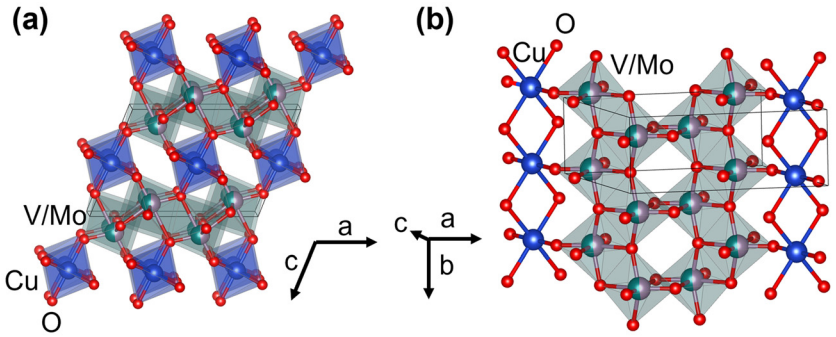

Fig. 1 (a) Polyhedral drawing of the unit cell view of the structure of $CuVMoO_6$ (**1**) and (b) a view with the *b*-axis vertical showing the extended connectivity of the layer.

shown in Fig. 1b, which is then further bridged to neighboring zigzag chains *via* edge-sharing into $[VMoO_6]^{n-}$ layers. A non-constrained refinement of the V1/Mo1 positions gives occupancies of 51.7(7)% V1 and 48.3(7)% Mo1, which is statistically within error of the idealized $CuVMoO_6$ composition. The anionic charge on these layers is balanced by the octahedrally-coordinated Cu cations located between them, Fig. 1a. Octahedral coordination of the Cu-cation is relatively rare for Cu(I)-containing oxides, consisting here of short Cu–O distances at 1.945(3) Å (×2) and longer distances at 2.377(2) (×4). Thus, it can be considered to be in a predominantly linear O–Cu–O coordination, but with four relatively longer Cu–O distances. This pattern of two short and four longer Cu–O distances has previously been found in Cu(I)-molybdates reported for $Cu_4Mo_5O_{17}$, $Cu_6Mo_5O_{18}$ and $CuSbMo_2O_8$,[27–29] but not reported for any Cu(I)-vanadates or related solid solutions.

Bond valence sum (BVS) calculations were performed to probe the oxidation states of the Cu, Mo, and V cations in **1**, as established by Brown and Altermatt and further refined for oxides.[30,31] The results are listed in Table 2. For the Cu-cation, the two shortest Cu–O distances give a partial BVS of +0.72, and when combined with the four longer Cu–O distances, give a net BVS of +1.1. This is consistent with a Cu(I) cation in a highly-distorted octahedral coordination environment. Conversely, the BVS values of the Mo and V cations result in values of +6.2 and +4.7, respectively. As both cations occupy the same crystallographic site, and therefore possess equivalent interatomic distances, these BVS values represent a relatively good fit for both types of cations. These values suggest that the Mo–O distances are typically expected to be a little longer, while the V–O distances would typically be expected to be somewhat shorter. However, the measured atomic positions represent the spatial average throughout the crystal structure and do not reflect the more subtle deviations that must be occurring around each type of atom. In summary, these interatomic distances represent a balance between the ideal distances for the preferred coordination of the respective V(V) and Mo(VI) oxidation states.

Table 2 Calculated bond valence sums for transition-metal cations in **1**, **2** and **3**

Compound	Element	BVS	Element	BVS	Element	BVS
1	Cu1	1.1	V1	4.7	Mo1	6.2
2	Cu1	0.9	V1	4.7	Mo1	6.2
2	Cu2	1.2	V2	4.9	Mo2[a]	6.5
3	Cu1	0.9	V1	4.7	W1	6.4
3	Cu2	1.2	V2	4.9	W2[a]	6.8

[a] These hypothetical positions did not show mixed occupancies with V in the refined crystal structures.

By comparison, a reaction loaded with a significantly smaller amount of Cu_2O and MoO_3 yielded compound **2**, with the structure illustrated in Fig. 2. In contrast to **1**, the isostructural W-containing version could be synthesized as well. Briefly, the structure of **2** contains layers with the nominal composition of $[V_{4-x}Mo_xO_{11}]^{-2+x}$ ($x \sim 0.40$ to 0.43) and comprised of two symmetry-unique V/Mo cation sites. The first crystallographic site is partially occupied by both V and Mo, *i.e.*, V1/Mo1, and is coordinated in a highly distorted octahedron with (V/Mo)–O distances of 1.663(5) Å, 1.8134(9) Å, 1.896(1) Å (×2), 2.148(5) Å and 2.232(5) Å. The second site is entirely occupied by V, *i.e.*, V2, and is coordinated in a distorted octahedral environment at slighter shorter distances of 1.627(5) Å, 1.737(5) Å, 1.910(1) Å (×2), 2.130(4) Å and 2.421(5) Å. These latter V2 octahedra are edge-shared to form zigzag chains, like that described above for **1**, but with further augmentation by vertex-shared O atoms to the chains of V1/Mo1-centered octahedra. A non-constrained refinement of the V1/Mo1 position gives occupancies of 78.3(9)% V1 and 21.7(9)% Mo1, which gives a nominal charge on the layer of −1.57. This anionic charge on the layer is balanced by the intra-layer Cu cations, as described by the two symmetry-unique positions of Cu1 and Cu2 as shown in Fig. 2b. The latter Cu cation, Cu2, is coordinated by two short Cu–O distances of 1.890(5) Å (×2) and four longer distances at 2.392(3) (×4), analogous with the structure of **1**. However, it also possesses a second Cu cation site, Cu1, that is coordinated in a distorted tetrahedral environment with Cu–O distances in the range of 1.953(6) Å to 2.284(6) Å. This latter position refines to an occupancy of 25.3(5)%.

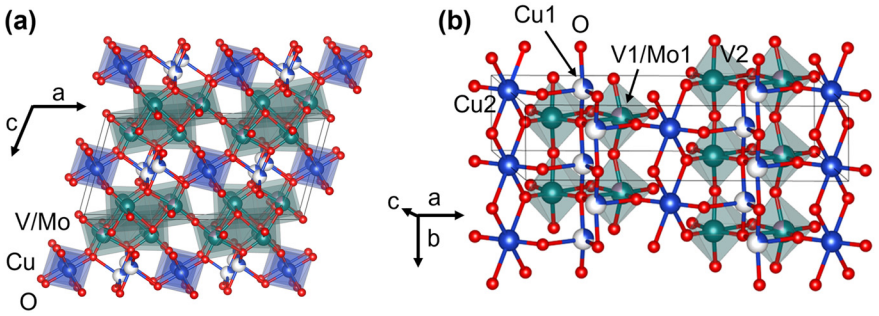

Fig. 2 (a) Polyhedral drawing of the unit cell view of the structure of $Cu_{1.51(1)}V_{3.57(1)}Mo_{0.43(1)}O_{11}$ (**2**) and (b) a view with the *b*-axis vertical showing the extended connectivity of the layer.

Assuming a +1 oxidation state for Cu1 and Cu2, the refined occupancy balances the net formal charge on the $[V_{4-x}Mo_xO_{11}]^{-2+x}$ layer. Given the Cu-disordered structure, this compound may potentially be an intermediate during the formation of **1**, as given by the following reaction: $Cu_3V_7MoO_{22}$ (**2**; idealized) + $6MoO_3$ + $2Cu_2O$ → $7CuVMoO_6$ (**1**). However, while the W version of **2** could be synthesized with similar Cu-site occupancies and V/W disorder, the hypothetical $CuVWO_6$ could not be prepared. This finding is further analyzed below with the use of density functional theory calculations.

As described above for **1**, the bond valence sums (BVS) for the cations in **2** and **3** were also calculated to assess the oxidation states of the Cu, Mo, W, and V cations. As shown listed in Table 2, both types of Cu-cation sites gave reasonable BVS values consistent with +1 oxidation states. In contrast to **1**, two types of V sites occur in the structures of **2** and **3**. The first crystallographic position, V1, exhibits mixed occupancy with either Mo1 in **2** or W1 in **3**. In these cases, the BVS of the Mo and V cations result in values of +6.2 and +4.7, and for the W and V cations of +6.4 and +4.7. These values match well with those also calculated for the structure of **1**, and thus are consistent with the expected +6 and +5 oxidation states for Mo/W and V, respectively. By contrast, the second crystallographic position, V2, does not show mixed occupancy with either Mo in **2** or W in **3** (highlighted in red in Table 2). Thus, the calculated BVS are not consistent with the expected oxidation states of Mo and W cations at +6.5 and +6.8, respectively. Thus, the presence of mixed V/Mo or V/W occupancies on only one of the two possible crystallographic sites can be understood as resulting from interatomic distances that either can or cannot accommodate both oxidation states. In short, only the interatomic distances for the V1/Mo1 site in **2** or the V1/W1 site in **3** provide for a suitable balance of distances to accommodate the dual-metal-cation occupation.

3.2. Electronic structure and optical properties

The paucity of reported Cu(I)-based semiconductors likely stems from their relative thermodynamic instability compared to their constituent binary oxides. Their decomposition energies (at 0 K) can be calculated using density-functional theory calculations with an accuracy of ~0.024 eV per atom.[32] As tabulated in the Materials' Project Database,[33] multinary Cu(I)-oxides containing early transition-metal cations, such as V, Ta, or Mo, are all shown to be thermodynamically unstable with respect to the binary oxides (ΔE_{rxn}) by −0.020 to −0.050 eV per atom. Typically, it is considered that thermodynamically-unstable compounds with energies less than about 100 meV per atom above the convex hull are potentially synthesizable, though strategies involving cation-exchange reactions have been demonstrated to push this empirical boundary.[34,35] As an example, both Cu_3VO_4 and $Cu_4Mo_5O_{17}$ are thermodynamically unstable and decompose to stoichiometric amounts of Cu_2O and V_2O_5 or MoO_3, respectively, with calculated ΔE_{rxn} for each of −0.107 eV per atom and −0.032 eV per atom. While each compound can be synthesized and isolated in high purity, they decompose upon heating at higher temperatures. It has remained a scientific conundrum as to whether any multinary Cu(I)-oxides could be synthesized that exhibited thermodynamic stability, and if not, why not?

Electronic structure calculations were carried out on **1**, **2** and **3** using density functional theory methods to assess the relative thermodynamic stabilities of these first known Cu(I)-molybdovanadates and Cu(I)-tungstovanadate. Their disordered structures were simulated using the superstructure approach. For compounds **2** and **3**, the partial occupancy of the Cu1 site (Fig. 2b) could be located across a shared bridge to either the Mo/W cation or the V cation and defining the two simulated α and β polymorphs of each structure. An example of each is drawn in Fig. S13 in the SI. Listed in Table 3 are the results of the calculated total energies of **1**, **2**, **3** and hypothetical "$CuVWO_6$", and their relatively thermodynamic stabilities *versus* the constituent binary oxides. All synthesized compounds are calculated to be lower than or very close to the convex hull of stability, within ±0.007 eV per atom, with stability *versus* the binary oxides in the order of **2** > **3** > **1** (when averaging the α and β of both **2** and **3**). Also, the α polymorph is slightly higher in energy than the β polymorph, but within error of each other. Thus, there is an absence of an energetic driving force for the ordering of the Cu(I) cation in the structures of **2** and **3**. Conversely, the hypothetical "$CuVWO_6$", is calculated to be thermodynamically unstable with respect to the binary oxides by −0.032 eV per atom, which is consistent

Table 3 Calculated total energies and relative stabilities of the quaternary Cu(I) oxides

Compound	Total energy (eV per atom)	Constituent binary oxides	Relative total energy[a] (eV per atom)
$CuVMoO_6$ (**1**)	−7.7600	$\frac{1}{2}$ Cu_2O, $\frac{1}{2}$ V_2O_5, MoO_3	−0.004
"$CuVWO_6$"	−8.0393	$\frac{1}{2}$ Cu_2O, $\frac{1}{2}$ V_2O_5, WO_3	−0.032
$Cu_3V_7MoO_{22}$ (**2**, α)	−7.8764	$1\frac{1}{2}$ Cu_2O, $3\frac{1}{2}$ V_2O_5, MoO_3	0.003
$Cu_3V_7MoO_{22}$ (**2**, β)	−7.8802	$1\frac{1}{2}$ Cu_2O, $3\frac{1}{2}$ V_2O_5, MoO_3	0.007
$Cu_3V_7WO_{22}$ (**3**, α)	−7.9567	$1\frac{1}{2}$ Cu_2O, $3\frac{1}{2}$ V_2O_5, WO_3	−0.001
$Cu_3V_7WO_{22}$ (**3**, β)	−7.9607	$1\frac{1}{2}$ Cu_2O, $3\frac{1}{2}$ V_2O_5, WO_3	0.003

[a] The relative total energies are calculated with respect to the listed constituent binary oxides. Negative and positive values correspond to thermodynamic stability or instability, respectively.

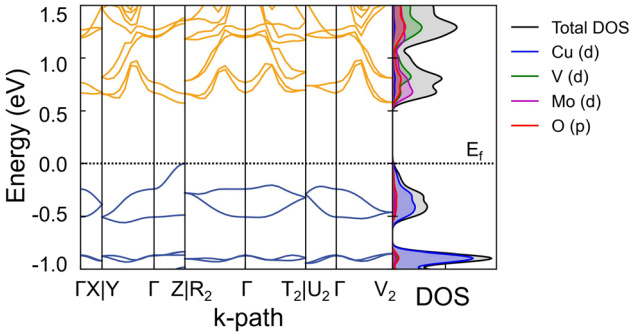

Fig. 4 Calculated density-of-states (DOS; right) and band structure (left) for **1** with the Fermi level (E_f) set at 0 eV and the individual atomic contributions projected out by orbital type.

with the failure of all synthetic attempts to prepare it. Its instability likely originates from a slightly greater size discrepancy between the V(V) and W(VI) cations and their relatively greater incompatibility to adopt the disordered arrangement exhibiting equivalent crystallographic sites. This aspect is also reflected in the greater discrepancy of their bond-valence sums, as described above. Thus, **1**, **2** and **3** represent the first quaternary Cu(I)-oxides calculated to occur below the thermodynamic convex hull (or within error) of stability.

As described above, an underlying motivation for the synthesis and study of Cu(I)-containing oxides has been their potential as semiconductors for applications involving solar energy conversion.[1–4] The low-energy limit for absorption of solar energy is set by the intrinsic bandgap of the semiconductor, with small bandgaps (E_g of about 0.9 to 1.5 eV) representing an ideal balance for utilization in tandem cells for solar-to-hydrogen conversion to capture the widest range of solar energy.[36] The majority of known Cu(I)-based semiconductors exhibit relatively larger bandgaps at >2.0 eV, with the exception of a few Cu(I)-niobates and vanadates.[13,14] Solid-state UV-Vis-NIR diffuse reflectance data were measured on polycrystalline $CuVMoO_6$ (**1**) between a wavelength range of 250 to 2000 nm. The results are given in the form of Tauc plots, depicted in Fig. 3. The direct band transition was found to be about 0.8(1) eV, while evidence for an indirect band transition could not be detected to approximately 0.5 eV owing to the detector's limits. Reported examples among the Cu(I)-vanadate and Cu(I)-molybate systems include only Cu_3VO_4 (E_g of about 1.2 eV).[8] Its small bandgap has been attributed to a combination of the high-energy $3d^{10}$-orbitals of the Cu(I) cation with the low-energy empty $3d^0$-orbitals of the V(V) cations, which respectively comprise the edge states of the valence band (VB) and conduction band (CB). By comparison, $Cu_{1.51(1)}V_{3.57(1)}Mo_{0.43(1)}O_{11}$ (**2**) and $Cu_{1.59(1)}V_{3.52(1)}W_{0.48(1)}O_{11}$ (**3**) were beyond the lower detection limit and could not be obtained in sufficiently high purity. These represent the smallest bandgaps among the wider range of Cu(I)-based systems.

The density-of-states (DOS), band structures and individual atomic-orbital contributions to the electronic structures were calculated to probe the origin of the small bandgaps of **1**, **2** and **3**. The results are shown in Fig. 4 and 5, with the results for the hypothetical "$CuVWO_6$" provided in the SI. For **1**, the edge states of its VB and CB derive predominantly from the Cu-based $3d^{10}$-states with an admixture of empty V($3d^0$) and Mo ($4d^0$) states, with the latter predominating at lower ener-

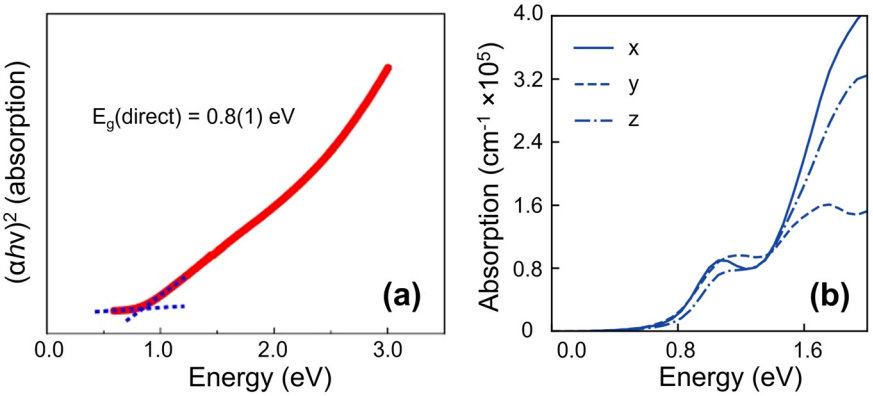

Fig. 3 Tauc plot of the direct band transition for **1** (a) and its calculated anisotropic optical absorption coefficient (b), with both plots *versus* energy in eV.

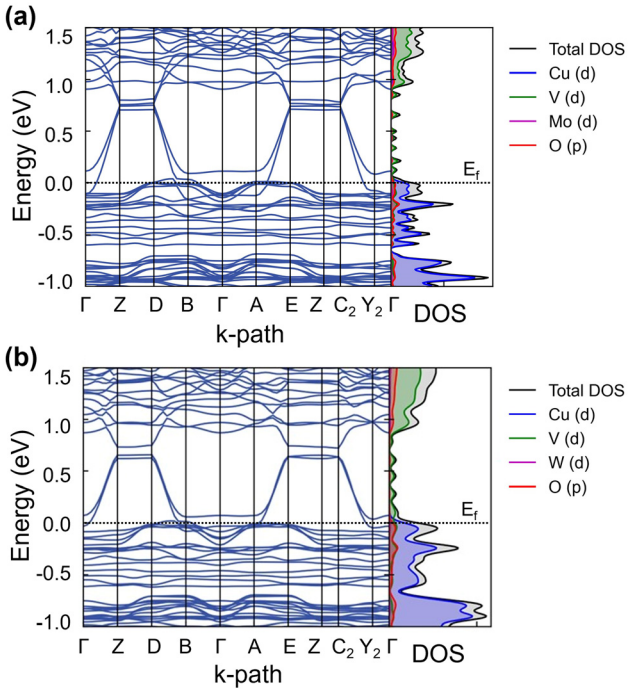

Fig. 5 Calculated density-of-states (DOS) and band structures for **2** (a) and **3** (b) with the Fermi levels (E_f) labeled at 0 eV and the individual atomic contributions projected out by orbital type.

gies. The bandgap is calculated to be ~0.57 eV and direct (Z-point), and somewhat lower than the experimental value. This is consistent with the under-estimation of semiconductor bandgaps using density functional theory calculations, which is a well-documented trend.[37] The optical absorption coefficient was calculated from the imaginary component of the dielectric function, as determined by the transition matrix elements. The results are shown in Fig. 3b for the three crystallographic directions of the structure. At only ~0.2 eV above the bandgap, the absorption coefficient rises steeply above 10^5 cm^{-1}. The [100] and [001], or x and z crystallographic directions, exhibit larger absorption values. This arises from the charge transfer Cu-to-V charge nature of the bandgap transition and the occurrence of O–Cu–O–V/Mo–O connectivity in these directions, as shown in Fig. 1. By contrast, this connectivity is absent in the [010] direction, as reflected in its relatively lower absorption values. Additionally, the optical absorption rises in two stages, corresponding respectively to the shallower and deeper Cu $3d^{10}$ states within the VB, Fig. 4, located between 0.0 and −1.0 eV. This large absorption coefficient is competitive with thin film semiconductors used for light capture and conversion but occurs at lower energy wavelengths. The hypothetical tungstate analogue, "$CuVWO_6$", shows an analogous electronic structure, Fig. S8 in the SI, with a few important differences. While the edge states of its VB is derived from Cu($3d^{10}$)-states, the CB edge consists predominantly of V($3d^0$)-states. The contributing W($5d^0$)-states occur much higher in energy as compared to Mo($4d^0$)-states in **1**. This leads to a larger calculated bandgap of about 0.66 eV and decreased thermodynamic stability, as described below.

Shown in Fig. 5, the electronic structures of **2** and **3**, by contrast, do not exhibit a clear energy gap at the Fermi level (E_f) and are thus inconsistent with semiconductor-like properties. The Fermi levels delineate a relatively gradual transition between filled Cu($3d^{10}$) states and empty Mo($4d^0$) or V($5d^0$) states in **2** and **3**, respectively, but with no clear energy gaps. The band structures of both show the Cu-based bands are relatively flat, while the Mo- and V-based bands are highly dispersed along directions aligned with the molybdovanadate and tungstovanadate chain directions. Intriguingly, these lowest-energy bands in the CB exhibit a rapid decrease and then very slightly touch and cross over the flatter Cu-based bands near the Fermi level. This band crossover occurs in momentum space, *i.e.*, *k*-space in Fig. 5, in areas both overlapping (Γ → Z) and separate (A → E), and predicting both **2** and **3** exhibit semi-metallic behavior. The band crossings imply potential for a slight oxidation of the Cu(I) cations, as probed below.

Analyses of the local bonding characters, *e.g.*, for the Cu–O, Mo/V–O and Cu–Cu pairwise interactions, were conducted to gain deeper insights into the underlying structural features

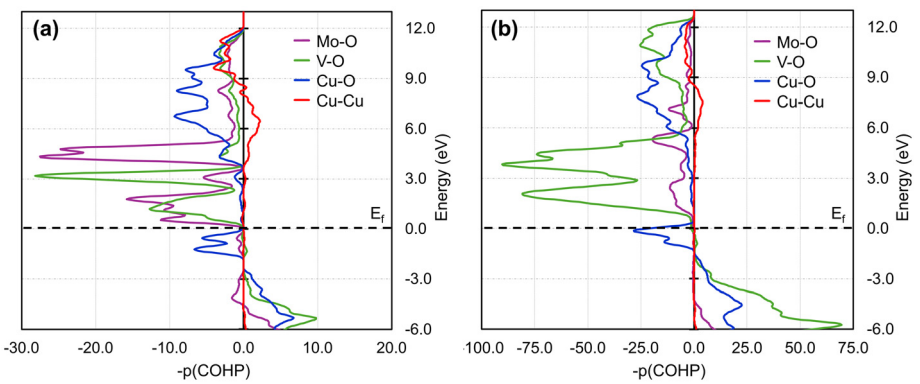

Fig. 6 Calculated Crystal Orbital Hamilton Populations (COHP) for the Mo–O, V–O, Cu–O, and Cu–Cu interactions for **1** (a) and **2** (b; β polymorph) with the Fermi levels (E_f) given as dashed lines at 0 eV. Positive and negative values indicate bonding and antibonding interactions, respectively.

leading to their relative stabilities and bandgaps. The Crystal Orbital Hamilton Populations (COHP) were calculated to obtain a measure of the bonding and antibonding interactions as a function of energy for the structures of **1**, **2** and **3**. The results are plotted in Fig. 6 for the structures of **1** (a) and **2** (b; in the β polymorph). These plots show predominantly bonding interactions, or positive COHP values, for Mo–O and V–O below the Fermi levels in each. By contrast, the Cu–O interactions shift from bonding to antibonding, or negative COHP values, for states closer to the Fermi level. These plots indicate that the VB edges of each structure are comprised predominantly of Cu–O antibonding states. Conversely, the CB states above the Fermi level consist of antibonding Mo–O, V–O, and Cu–O interactions for both structures. The Cu–Cu interactions are negligibly weak by comparison. These trends in the COHP curves are consistent across the other structures of **3** (both polymorphs) and the hypothetical 'CuVWO6' compound, as found in the SI in Fig. S9 to S12.

A closer analysis of the frontier energy levels at the VB edges for the Cu–O antibonding interactions reveal important differences that likely impacts their thermodynamic stability. In comparing the COHP curves for **1** and **2**, illustrated in Fig. 6 (blue lines in panels a and b), the latter has Cu–O antibonding interactions that are shifted to higher energies. This leads to partial depopulation, *i.e.*, oxidation, of these antibonding states in **2**. This is offset by a partial population of the V–O antibonding states that fall slightly below the Fermi level. These same trends are found for **3** in Fig. S11 (SI), with the net effect that there is relatively little impact on their relatively thermodynamic stability *versus* the binary oxides. By contrast, the Cu–O COHP curves for the hypothetical "$CuVWO_6$" *versus* **1** ($CuVMoO_6$) shows a more significant difference, as plotted together in Fig. 7 *versus* energy. The hypothetical "$CuVWO_6$" shows a significant shifting of the antibonding Cu–O interactions at the VB edge to higher energies. As a result, its calculated thermodynamic stability is decreased (Table 3), consistent with the inability to synthesize it during the synthetic trials under various reaction conditions. The underlying reason for this can be traced to a secondary effect of the Mo/W–O–Cu interactions. In brief, the relatively higher energy $W(5d^0)$-states interact relatively more weakly with the filled O-2p states because of their greater energetic separation, thus causing the O-2p states to shift to relatively higher energies. As a result, the Cu-3d and O-2p based states are relatively closer in energy in "$CuVWO_6$", and shifting the Cu–O antibonding interactions to higher energies near the Fermi level. Most interestingly, this finding suggests that new quaternary Cu(I)-oxides may be stabilized and discovered with the incorporation of early transition-metal cations with relatively lower-energy d orbitals.

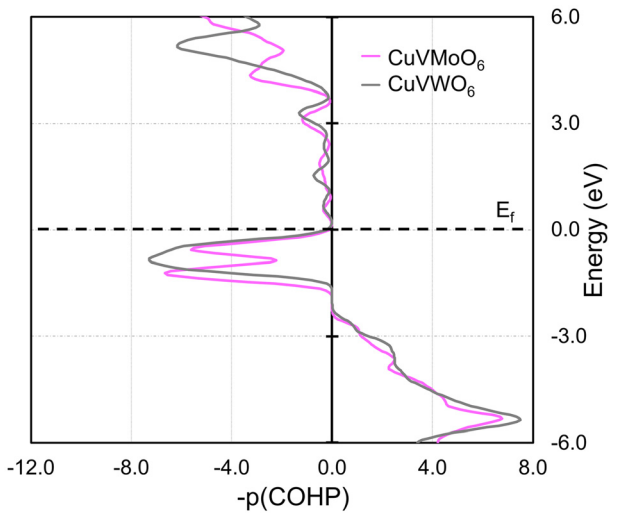

Fig. 7 Calculated Crystal Orbital Hamilton Populations (COHP) for the Cu–O interactions for $CuVMoO_6$ (**1**) and $CuVWO_6$ with the Fermi levels (E_f) at 0 eV.

4. Conclusions

Synthetic explorations of the Cu(I)–V(V)–M(VI)–O (M = Mo, W) have resulted in the discovery of two new Cu(I)-molybdovanadates and a new Cu(I)-tungstovanadate compound. Their structures are comprised of mixed, disordered $(V/Mo)O_6$ or $(V/W)O_6$ sites as well as associated Cu-site vacancy disorder. Generally, their structures feature layers of these highly distorted VO_6/MO_6 octahedra, with the interlayer sites partially occupied by Cu(I) cations in either tetrahedral or in uncommon distorted-octahedral geometries. Density functional calculations were used to assess their bandgaps and thermodynamic stabilities *versus* the binary oxides. While **1** exhibits a small direct band transition of ~0.8 eV, both **2** and **3** are calculated to be semimetals without an energy gap. The latter display relatively large band dispersions in their CB states and leads to a partial de-population of the Cu–O antibonding states. In turn, this yields a relatively greater thermodynamic stability *versus* the binary oxides, which represents a rare feature among known multinary Cu(I) oxides. Conversely, the hypothetical "$CuVWO_6$" compound was calculated to be thermodynamically unstable owing to relatively higher energy Cu–O antibonding interactions and could also not be synthesized in this work. Also, in comparison to prior reported ternary and quaternary Cu(I) oxides,[6–14] the coordination of the Cu(I) cation in a linear or tetrahedral coordination geometry appears to be key to achieving wider bandgaps. Thus, these results reveal a deeper understanding of new approaches to prepare thermodynamically-stable Cu(I) oxides with suitably sized bandgaps for utility in future applications involving solar energy conversion.

Conflicts of interest

There are no conflicts to declare.

Data availability

The data underlying the electronic structure calculations are openly available in the Materials Cloud repository at https://doi.org/10.24435/materialscloud:71-cw.

Supplementary information: characterization data including the powder XRD patterns, EDX spectra, and results of electronic structure calculations. See DOI: https://doi.org/10.1039/d5dt02255j.

CCDC 2444829 (**1**) and 2444831 (**2**) and 2444832 (**3**) contain the supplementary crystallographic data for this paper.[39a–c]

Acknowledgements

The authors acknowledge primary support of this work from the National Science Foundation (DMR-2317605 and DMR-2516105). The data underlying the electronic structure calculations have been made openly available in the Materials Cloud repository at https://doi.org/10.24435/materialscloud:71-cw. This work used the High-Performance Research Computing FASTER cluster at Texas A&M University through allocation CHE240107 from the Advanced Cyberinfrastructure Coordination Ecosystem: Services & Support (ACCESS) Program,[38] which is supported by U.S. National Science Foundation grants #2138259, #2138286, #2138307, #2137603, and #2138296.

References

1 I. Sullivan, B. Zoellner and P. A. Maggard, Copper(I)-Based p-Type Oxides for Photoelectrochemical and Photovoltaic Solar Energy Conversion, *Chem. Mater.*, 2016, **28**(17), 5999–6016.

2 S. D. Tilley, Will Cuprous Oxide Really Make It in Water-Splitting Applications?, *ACS Energy Lett.*, 2023, **8**(5), 2338–2344.

3 A. Köche, K. T. Hong, S. Seo, F. Babbe, H. Gim, K. H. Kim, H. Choi, Y. Jung, I. Oh, G. V. Krishnamurthy, M. Stömer, S. Lee, T.-H. Kim, A. T. Bell, S. Khan, C. M. Sutter-Fella and F. M. Toma, Copper Tantalate by a Sodium-Driven Flux-Mediated Synthesis for Photoelectrochemical CO_2 Reduction, *Small Methods*, 2025, 2401432.

4 J. de Almeida, S. H. Câmara, R. Bertazzoli, K. Rajeshwar, R. A. G. da Silva and C. D. Rodrigues, Selective Photoelectrocatalytic CO_2 Reduction to Ethanol Using Nanotubular Oxides Grown on Metastable Ti-Cu alloy, *Chem. Eng. J.*, 2023, **477**, 147117.

5 C. M. Jiang, S. E. Reyes-Lillo, Y. F. Liang, Y. S. Liu, G. J. Liu, F. M. Toma, D. Prendergast, I. D. Sharp and J. K. Cooper, Electronic Structure and Performance Bottlenecks of $CuFeO_2$ Photocathodes, *Chem. Mater.*, 2019, **31**, 2524–2534.

6 B. Zoellner, S. Stuart, C. C. Chung, D. B. Dougherty, J. L. Jones and P. A. Maggard, $CuNb_{1(-x}Ta_xO_3$ ($x \leq 0.25$) Solid Solutions: Impact of Ta(V) Substitution and Cu(I) Deficiency on Their Structure, Photocatalytic, and Photoelectrochemical Properties, *J. Mater. Chem. A*, 2016, **4**, 3115–3126.

7 P. A. Maggard, Capturing Metastable Oxide Semiconductors for Applications in Solar Energy Conversion, *Acc. Chem. Res.*, 2021, **54**, 3160–3171.

8 P. P. Sahoo, B. Zoellner and P. A. Maggard, Optical, Electronic, and Photoelectrochemical Properties of the p-Type $Cu_{3-x}VO_4$ Semiconductor, *J. Mater. Chem. A*, 2015, **3**, 4501–4509.

9 S. O'Donnell, R. K. Kremer and P. A. Maggard, Metastability and Photoelectrochemical Properties of Two Cu(I)-Based Oxides with Delafossite Structures, *Chem. Mater.*, 2023, **35**, 1404–1416.

10 M. T. Galante, A. Zivkovic, J. C. Alvim, C. C. C. Kleiner, M. Sangali, S. F. R. Taylor, A. J. Greer, C. Hardacre, K. Rajeshwar, R. Caram, R. Bertazzoli, R. T. Macaluso, N. H. de Leeuw and C. Longo, Arc Synthesis, Crystal Structure, and Photoelectrochemistry of Copper(I) Tungstate, *ACS Appl. Mater. Interfaces*, 2021, **13**, 32865–32875.

11 I. Sullivan, P. P. Sahoo, L. Fuoco, A. S. Hewitt, S. Stuart, D. Dougherty and P. A. Maggard, Cu-Deficiency in the p-Type Semiconductor $Cu_{5-x}Ta_{11}O_{30}$: Impact on its Crystalline Structure, Surfaces, and Photoelectrochemical Properties, *Chem. Mater.*, 2014, **26**, 6711–6721.

12 N. King, J. Boltersdorf, P. A. Maggard and W. Wong-Ng, Polymorphism and Structural Distortions of Mixed-Metal Oxide Photocatalysts Constructed with α-U_3O_8 Types of Layers, *Crystals*, 2017, **7**, 145.

13 N. King, P. P. Sahoo, L. Fuoco, S. Stuart, D. Dougherty, Y. Liu and P. A. Maggard, Copper Deficiency in the p-Type Semiconductor $Cu_{1-x}Nb_3O_8$, *Chem. Mater.*, 2014, **26**, 2095–2104.

14 J. Choi, N. King and P. A. Maggard, Metastable Cu(I)-Niobate Semiconductor with a Low-Temperature Nanoparticle-Mediated Synthesis, *ACS Nano*, 2013, **7**, 1699–1708.

15 Agilent, *Crysalis PRO*, Agilent Technologies Ltd, Yarnton, Oxfordshire, England, 2014.

16 G. M. Sheldrick, A short history of SHELX, *Acta Crystallogr., Sect. A:Found. Crystallogr.*, 2008, **64**, 112–122.

17 A. L. Spek, Single-crystal structure validation with the program PLATON, *J. Appl. Crystallogr.*, 2003, **36**, 7–13.

18 L. M. Gelato and E. Parthe, Structure Tidy - a Computer-Program to Standardize Crystal-Structure Data, *J. Appl. Crystallogr.*, 1987, **20**, 139–143.

19 G. Kortüm and J. E. Lohr, *Reflectance Spectroscopy: Principles, Methods, Applications*, Springer Berlin Heidelberg, 2012.

20 P. Makuła, M. Pacia and W. Macyk, How To Correctly Determine the Band Gap Energy of Modified Semiconductor Photocatalysts Based on UV–Vis Spectra, *J. Phys. Chem. Lett.*, 2018, **9**, 6814–6817.

21 G. Kresse and J. Furthmuller, Efficiency of Ab initio Total Energy Calculations for Metals and Semiconductors Using a Plane-Wave Basis Set, *Comput. Mater. Sci.*, 1996, **6**, 15–50.
22 G. Kresse and J. Furthmuller, Efficient Iterative Schemes for Ab Initio Total-Energy Calculations Using a Plane-Wave Basis Set, *Phys. Rev. B:Condens. Matter Mater. Phys.*, 1996, **54**, 11169–11186.
23 Y. Hinuma, G. Pizzi, Y. Kumagai, F. Oba and I. Tanaka, Band Structure Diagram Paths Based on Crystallography, *Comput. Mater. Sci.*, 2017, **128**, 140–184.
24 R. Dronskowski and P. E. Bloechl, Crystal orbital Hamilton populations (COHP). Energy-resolved Visualization of Chemical Bonding in Solids Based on Density-Functional Theory Calculations, *J. Phys. Chem.*, 1993, **97**, 8617–8624.
25 S. Maintz, V. L. Deringer, A. L. Tchougréeff and R. Dronskowski, LOBSTER: A Tool to Extract Chemical Bonding from Plane-Wave Based DFT, *J. Comput. Chem.*, 2016, **37**, 1030–1035.
26 R. Nelson, C. Ertural, J. George, V. L. Deringer, G. Hautier and R. Dronskowski, LOBSTER: Local Orbital Projections, Atomic Charges, and Chemical-Bonding Analysis from Projector-Augmented-Wave-Based Density-Functional Theory, *J. Comput. Chem.*, 2020, **41**, 1931–1940.
27 E. M. McCarron III and J. C. Calabrese, Synthesis and, Structure of $Cu^{1+}{}_4Mo^{6+}{}_5O_{17}$, *J. Solid State Chem.*, 1986, **15**, 215–224.
28 M. Koop and H. k. Müller-Bushbaum, Synthesis and Crystal-Structure of $Cu_6Mo_5O_{18}$, *Z. Anorg. Allg. Chem.*, 1985, **531**, 140–146.
29 H. Szillat and H. k. Müller-Bushbaum, On the Synthesis and Crystal Structure of a New Copper Antimony Oxomolybdate: $CuSbMo_2O_8$, *Z. Naturforsch., B:J. Chem. Sci.*, 1995, **50**, 717–720.
30 I. D. Brown and D. Altermatt, Bond-Valence Parameters Obtained from a Systematic Analysis of the Inorganic Crystal Structure Database, *Acta Crystallogr., Sect. B:Struct. Sci.*, 1985, **41**, 244–247.
31 O. C. Gagné and F. C. Hawthorne, Comprehensive Derivation of Bond-Valence Parameters for Ion Pairs Involving Oxygen, *Acta Crystallogr., Sect. B:Struct. Sci., Cryst. Eng. Mater.*, 2015, **71**, 562–578.
32 G. Hautier, S. P. Ong, A. Jain, C. J. Moore and G. Ceder, Accuracy of Density Functional Theory in Predicting Formation Energies of Ternary Oxides from Binary Oxides and Its Implications on Phase Stability, *Phys. Rev. B: Condens. Matter Mater. Phys.*, 2012, **85**, 155028.
33 A. Jain, S. P. Ong, G. Hautier, W. Chen, W. D. Richards, S. Dacek, S. Cholia, D. Gunter, D. Skinner, G. Ceder and K. A. Persson, Commentary: The Materials Project: A Materials Genome Approach to Accelerating Materials Innnovation, *APL Mater.*, 2013, **1**, 011002.
34 M. Aykol, S. S. Dwaraknath, W. Sun and K. A. Persson, Thermodynamic Limit for Synthesis of Metastable Inorganic Materials, *Sci. Adv.*, 2018, **4**, eaaq0148.
35 S. O'Donnell, C. C. Chung, A. Carbone, R. Broughton, J. L. Jones and P. A. Maggard, Pushing the Limits of Metastability in Semiconducting Perovskite Oxides for Visible-Light-Driven Water Oxidation, *Chem. Mater.*, 2020, **32**, 3054–3064.
36 S. O'Donnell, A. Vali, A. Rawat, P. A. Maggard, M. N. Huda and K. Rajeshwar, Perspective-Multinary Oxide Semiconductors for Solar Fuels Generation: Closing the Performance Gap Between Theory and Practice, *ECS J. Solid State Sci. Technol.*, 2022, 053001.
37 J. P. Perdew, Density Functional Theory and the Band Gap Problem, *Int. J. Quantum Chem.*, 1985, **28**, 497–523.
38 T. J. Boerner, S. Deems, T. R. Furlani, S. L. Knuth and J. Towns, ACCESS: Advancing Innovation: NSF's Advanced Cyberinfrastructure Coordination Ecosystem: Services & Support, in *Practice and Experience in Advanced Research Computing (PEARC '23)*, ACM, New York, NY, USA, Portland, OR, USA, 2023, 4 pages.
39 (*a*) CCDC 2444829: Experimental Crystal Structure Determination, 2025, DOI: 10.5517/ccdc.csd.cc2n21g8; (*b*) CCDC 2444831: Experimental Crystal Structure Determination, 2025, DOI: 10.5517/ccdc.csd.cc2n21jb; (*c*) CCDC 2444832: Experimental Crystal Structure Determination, 2025, DOI: 10.5517/ccdc.csd.cc2n21kc.